

# Dimensionality Transformation through Paddlewheel Reconfiguration in a Flexible and Porous Zn-Based Metal–Organic Framework

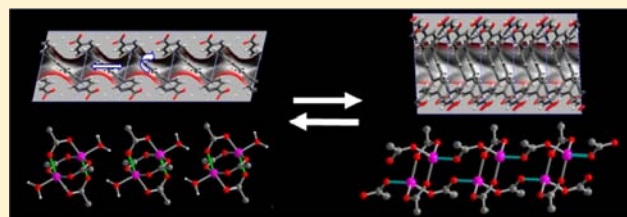
Kyriakos C. Stylianou,<sup>†</sup> Jeremy Rabone,<sup>†</sup> Samantha Y. Chong,<sup>†</sup> Romain Heck,<sup>†</sup> Jayne Armstrong,<sup>‡</sup> Paul V. Wiper,<sup>†</sup> Kim E. Jelfs,<sup>†</sup> Sergey Zlatogorsky,<sup>†</sup> John Bacsa,<sup>†</sup> Alec G. McLennan,<sup>†</sup> Christopher P. Ireland,<sup>†</sup> Yaroslav Z. Khimyak,<sup>†</sup> K. Mark Thomas,<sup>‡</sup> Darren Bradshaw,<sup>\*,†,§</sup> and Matthew J. Rosseinsky<sup>\*,†</sup>

<sup>†</sup>Department of Chemistry, University of Liverpool, Liverpool L69 7ZD, U.K.

<sup>‡</sup>Northern Carbon Research Laboratories, Sir Joseph Swan Institute and School of Chemical Engineering and Advanced Materials, Bedson Building, Newcastle University, Newcastle upon Tyne NE1 7RU, U.K.

## Supporting Information

**ABSTRACT:** The reaction between Zn and a pyrene-based ligand decorated with benzoate fragments (H<sub>4</sub>TBAPy) yields a 2D layered porous network with the metal coordination based on a paddlewheel motif. Upon desolvation, the structure undergoes a significant and reversible structural adjustment with a corresponding reduction in crystallinity. The combination of computationally assisted structure determination and experimental data analysis of the desolvated phase revealed a structural change in the metal coordination geometry from square-pyramidal to tetrahedral. Simulations of desolvation showed that the local distortion of the ligand geometry followed by the rotation and displacement of the pyrene core permits the breakup of the metal-paddlewheel motifs and the formation of 1D Zn–O chains that cross-link adjacent layers, resulting in a dimensionality change from the 2D layered structure to a 3D structure. Constrained Rietveld refinement of the powder X-ray diffraction pattern of the desolvated phase and the use of other analytical techniques such as porosity measurements, <sup>13</sup>C CP MAS NMR spectroscopy, and fluorescence spectroscopy strongly supported the observed structural transformation. The 3D network is stable up to 425 °C and is permanently porous to CO<sub>2</sub> with an apparent BET surface area of 523(8) m<sup>2</sup>/g (*p/p*<sup>o</sup> = 0.02–0.22). Because of the hydrophobic nature, size, and shape of the pores of the 3D framework, the adsorption behavior of the structure toward *p*-xylene and *m*-xylene was studied, and the results indicated that the shape of the isotherm and the kinetics of the adsorption process are determined mainly by the shape of the xylene isomers, with each xylene isomer interacting with the host framework in a different manner.



## INTRODUCTION

Microporous metal–organic frameworks (MOFs) derived from the self-assembly of metal ions or clusters known as secondary building units (SBUs) with multidentate organic ligands<sup>1–3</sup> are widely recognized as an important class of compounds with potential applications in gas storage,<sup>4–6</sup> separation,<sup>7–9</sup> catalysis,<sup>10–12</sup> drug delivery,<sup>13–15</sup> and molecular sensing.<sup>16–18</sup> MOFs are characterized by their tunable pore sizes, topologies, and functionality and their inherent flexibility<sup>19</sup> arising from their inorganic–organic hybrid nature, leading to their classification as soft porous crystals. Such flexibility is not generally observed in more classic carbon- or oxide-based porous materials. Framework flexibility usually occurs as a guest-induced transformation between two or more structures that occurs upon desolvation and/or guest readsorption.<sup>20</sup> Dynamic frameworks are typified by stepped and hysteretic sorption profiles that lead to guest-responsive behaviors<sup>21–24</sup> and the uptake of molecules that exceed the size of the

windows providing access to the pores.<sup>25</sup> In some cases, the guest-induced structural transformations that occur in dynamic frameworks can induce a sensory response if they also possess properties such as fluorescence<sup>26</sup> or magnetism.<sup>27</sup> A detailed understanding of these behaviors is thus important in the design of future materials for the applications outlined.

The most common causes of framework flexibility are motions of the relatively rigid organic ligand components. The typically aromatic ligands used in many MOFs act as freely rotating molecular rotors,<sup>28,29</sup> and their rotation, and hence access to the porosity, can be affected by temperature,<sup>30</sup> pressure,<sup>31</sup> or the presence of specific guests.<sup>32</sup> This latter property has been further exploited to prepare frameworks from functionalized pillaring ligands that act as molecular gates, which are “unlocked” only by guest molecules that disrupt the

Received: September 10, 2012

Published: November 5, 2012

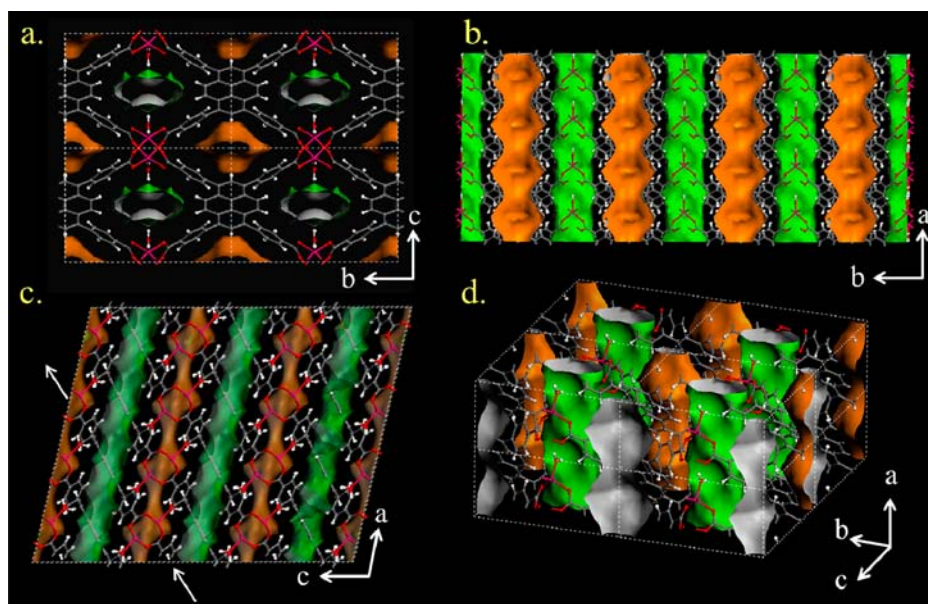


**Figure 1.** (a) Connolly surface representation of **1** viewed down the *a* axis. The coordination of four different TBAPy ligands to Zn paddlewheel units gives rise to a 2D network. (b) Illustration of **1** viewed down the *c* axis showing the formation of two distinct types of pores (colored in green and orange) running along the *a* axis. These channels have almost identical dimensions but differ in the chemical nature of the species lining them. (c) Stacking of the pyrene cores of the layers along the *b* axis affords a porous network; layers are pointed out with white arrows. (d) Connolly surface representation of the 2D-layered **1** in a 3D view. Atom colors: pink, Zn; gray, C; red, O; white, H.

hydrogen bonding between the side chains.<sup>33,34</sup> Ligand movements can also cause significant displacement of the inorganic SBUs that allow large breathing motions such as those observed in the carboxylate-based MIL-*n* frameworks, which can expand by up to 300%.<sup>35</sup> Framework dynamics can be predesigned in MOFs by employing inherently flexible ligands, such as the dipeptides used by Rabone et al.<sup>36</sup> Here the conformational flexibility of the ligands permits access to a continuum of low-energy states on the cusp of the materials disorder rather than simple open/closed binary switching as previously reported. Dynamic framework behaviors can also arise from the motion of whole networks relative to one another, such as the dislocation of interdigitated layers<sup>37</sup> or the displacement of interpenetrated three-dimensional (3D) nets.<sup>38</sup>

Framework dynamics and guest-responsive behavior can also be induced by a change in coordination number or geometry at the metal centers within MOFs, which can lead to a dimensionality change in the overall framework connectivity.<sup>39</sup> It is widely accepted that the SBU clusters used in MOF construction are relatively inert rigid units, but there are an increasing number of reports suggesting that these too have dynamic behaviors. For example, it has recently been demonstrated that the Zr clusters in UiO-66 materials can undergo dynamic ligand exchange,<sup>40</sup> and in situ studies have established that some SBUs can readily transform into a more stable arrangement during framework synthesis.<sup>41</sup> Among the common SBUs, the  $M_2(OAc)_4$  [ $M = \text{Cu(II)}, \text{Zn(II)}$ ] paddlewheel arrangement appears to be particularly labile and readily undergoes guest-molecule-induced dissociation and reconstruction in the solid state.<sup>34,42</sup> In this way, a two-dimensional (2D) layered coordination framework can be reversibly transformed into a 3D pts network upon addition/removal of water ligands,<sup>42</sup> and the internal paddlewheel rearrangement in the doubly interpenetrated pillared layer frameworks induces layer slippage and the displacement of the nets to generate a material with complex and selective porosity

that can be regenerated in the presence of  $\text{CO}_2$  guest species.<sup>34</sup> These two examples were fully characterized by single-crystal X-ray diffraction (XRD), but more often than not, framework flexibility causes a loss of long-range order that makes the identification of the structural architectures resulting from such dynamics difficult by diffraction alone. This is especially true when the natures of the SBUs in the two networks are fundamentally different in regard to connectivity. Computational methods are thus becoming increasingly important in this area, and we have recently demonstrated that combining simulations with experimental analytical data is a powerful strategy for structure determination of frameworks prepared from highly flexible ligands.<sup>36</sup>

Here we extend this approach to characterize the structural transformation of a 2D layered network based on Zn paddlewheel units and the ligand TBAPy<sup>4-</sup> [ $\text{H}_4\text{TBAPy} = 1,3,6,8\text{-tetrakis}(p\text{-benzoic acid})\text{pyrene}$ ] into a 3D porous network through cross-linking of the layers upon removal of the water molecules bound in the axial positions. Removal of the coordinated  $\text{H}_2\text{O}$  and other guest molecules produces a less crystalline material with significantly reduced long-range order. Molecular dynamics (MD) simulations revealed a change in the coordination geometry of Zn from square-pyramidal to tetrahedral, resulting in a framework that is extended in three dimensions and retains permanent porosity. These simulations allowed the development of a quantitative structural model in which the ligand can reorient flexibly to maintain permanent porosity by forming interlayer connections, affording one-dimensional (1D) chains of carboxylate-bridged tetrahedral Zn centers that increase the structural dimensionality. While dimensionality changes from 2D to 3D upon dehydration that induce changes in magnetic and optical properties have previously been observed for interdigitated layered frameworks,<sup>43</sup> this is the first time that such a transformation, as originally proposed by Li et al.<sup>44</sup> to account for the unexpected thermal stability of MOF-2, has been fully characterized in a

layered system constructed from Zn paddlewheels. This structural change is shown to control the functional optical and sorption response.

## EXPERIMENTAL SECTION

**General Information.** Reagents and solvents were purchased from Sigma-Aldrich and used as received without further purification.  $H_4TBAPy$  ( $C_{44}H_{26}O_8$ ) was synthesized as described elsewhere.<sup>26</sup> Elemental analyses (C, H, and N) were obtained using a Thermo Finnigan EA 1112 Flash CHNS-O analyzer. The powder XRD (PXRD) patterns of the as-made phase **1** and the samples loaded with xylene isomers were collected in transmission geometry using a STOE Stadi-P diffractometer with  $Cu K\alpha_1$  radiation at 298 K. The high-resolution PXRD pattern of the desolvated phase **1'** was collected on 0.5 mm diameter spinning capillaries at beamline I11 of the Diamond Light Source, U.K., at a wavelength of 0.82633 Å. Details of the experimental and theoretical procedures and methods used for desolvation; thermogravimetric analysis (TGA);  $^{13}C$  cross-polarization (CP) magic-angle-spinning (MAS) NMR spectroscopy; scanning electron microscopy (SEM); IR, UV–vis, and fluorescence spectroscopy; stability tests; simulations; gas sorption; and xylene loading can be found in the Supporting Information (SI).

**Synthesis of  $[Zn_2(TBAPy)(H_2O)_2] \cdot (Guests)_x$  (**1**).** To a suspension of  $Zn(NO_3)_2 \cdot 6H_2O$  (9 mg, 0.030 mmol) and  $H_4TBAPy$  (10 mg, 0.015 mmol) in *N,N*-dimethylformamide (DMF) (2.5 mL) were added dioxane (1.25 mL) and  $H_2O$  (1.25 mL) ( $V_{total} = 5$  mL) along with 10  $\mu L$  of HCl, and the resulting yellow solution was sonicated for 10 min. The resulting yellow suspension was heated to 120 °C for 72 h in a 12 mL sealed vial and then cooled to 30 °C at a rate of 0.2 °C/min. The resulting yellow block crystals were filtered and washed with 10 mL of the same mixture of solvents used for the synthesis. **1** was isolated in 41% yield based on Zn. Elemental analysis calculated for  $[Zn_2(C_{44}H_{22}O_8)(H_2O)_2] \cdot (C_4H_8O_2)_{1.5}(C_3NOH_7)_{0.5}(H_2O)_{1.1}$ : C, 59.98; H, 4.24; N, 0.67. Found: C, 60.15; H, 4.02; N, 0.76.

## RESULTS AND DISCUSSION

### Synthesis and Single-Crystal Structure Determination

**of **1**.** The reaction of  $H_4TBAPy$  with  $Zn(NO_3)_2 \cdot 6H_2O$  in an acidic 2:1:1 DMF–dioxane– $H_2O$  solvent mixture in a 12 mL sealed vial at 120 °C produced pale-yellow X-ray-quality single crystals of the 2D framework  $[Zn_2(TBAPy)(H_2O)_2] \cdot (guests)_x$  (**1**). **1** adopts a monoclinic structure (Table S1 in the SI) based on  $Zn_2(O_2C)_4$  paddlewheel units with axially coordinated water molecules (Figure 1a and Figure S1 in the SI). Each TBAPy ligand is coordinated to eight adjacent Zn atoms, with the benzoate groups appended at the 1-, 3-, 6-, and 8-positions of the pyrene core (Figure S2) coordinated in a bidentate bridging fashion, to form the observed 2D-layer-based porous network with 1D channels parallel to the crystallographic *a* axis (Figure 1b,c and Figure S3). The layers are stacked in an eclipsed manner along the *a* axis and aligned by 4.533(9) Å  $\pi$ – $\pi$  stacking interactions between the pyrene cores and hydrogen bonding between coordinated  $H_2O$  molecules and carboxylate oxygens [ $HO^{\delta-}H^{\delta+} \cdots O^{\delta-}C^{\delta+} = 2.358(1)$  Å; Figure S4]. There are two crystallographically distinct channels with almost identical maximum/minimum dimensions of 9.9 Å  $\times$  3.6 Å and 10.0 Å  $\times$  3.4 Å (colored green and orange, respectively, in Figure 1a; the pore dimensions were calculated with HOLE<sup>45</sup> including van der Waals radii), distinguished by being lined with coordinated water and aromatic groups, respectively. Connolly surface calculations performed using the Materials Studio 5.0 modeling package with a probe radius of 1.0 Å gave an accessible volume of 460 Å<sup>3</sup> per unit cell (39.3%). Combining the accessible volume and the density of the static structure of **1** (after

removal of the coordinated  $H_2O$  molecule) gave a pore volume of 0.274 cm<sup>3</sup>/g for **1**.

The channel interiors in **1** contain crystallographically disordered solvent molecules that show no indication of preferred location. Analysis of the residual electron density using the SQUEEZE function within the PLATON<sup>46</sup> suite of programs indicated the presence of 105 electrons, corresponding to approximately one of each solvent molecule used during synthesis of **1** (dioxane,  $H_2O$ , and DMF), in good agreement with the bulk formula determined from elemental analysis (see section 5 in the SI).

**Bulk Characterization.** The bulk phase and analytical purity of as-made **1** were confirmed by PXRD, elemental analysis (section 5 in the SI), TGA, and SEM. The Le Bail fit of  $[Zn_2(TBAPy)(H_2O)_2] \cdot (dioxane)_{1.5}(DMF)_{0.5}(H_2O)_{1.1}$  (**1**) gave the refined cell parameters  $a = 6.8229(2)$  Å,  $b = 15.7670(5)$  Å,  $c = 11.1900(3)$  Å,  $\alpha = \gamma = 90^\circ$ ,  $\beta = 102.922(2)^\circ$ , and  $V = 1173.36(3)$  Å<sup>3</sup> with excellent fit indicators ( $R_{wp} = 4.13\%$ ,  $R_p = 3.23\%$ ,  $\chi^2 = 1.31$ ) (Figure S5), in good agreement with the parameters obtained from the single-crystal structure determination. SEM images confirmed the homogeneity of **1** and revealed the blocklike morphology of the crystals (Figure S6). TGA showed that all of the extraframework guests and the coordinated  $H_2O$  molecules (total mass loss = 22.2%) were removed over the temperature range 120–240 °C within a single step (Figure S7), in agreement with the observed composition obtained from the microanalytical data (calcd 22.7%). Decomposition of the framework occurred above 425 °C.

**Structural Behavior of **1** upon Desolvation.** **1** was outgassed overnight at 110 °C under dynamic vacuum ( $10^{-5}$  mbar) to yield desolvated **1'**, where a color change from pale to dark-yellow was observed (Figure S8). The formula of **1'** was initially determined as  $Zn_2(TBAPy)$  by elemental analysis performed under inert conditions. The PXRD profile of **1'** indicates an extensive loss of crystalline order, as evidenced by reduced intensities and broadening of the majority of reflections, consistent with the deterioration and apparent delamination of the crystals observed by SEM (Figure S6). The remaining sharp diffraction intensities observed at low angles, with *d* spacings of 14.7 and 10.7 Å, correspond to separations of Zn centers in the structure (Figures S9 and S10). Initial attempts to index the pattern did not take into account the broad, diffuse intensity centered at  $\sim 8.4^\circ$ . Satisfactory Le Bail fits on **1'** (denoted by **1'LB-a**) were obtained by fitting this feature as part of the background intensity to give a triclinic cell:  $a_{1'LB-a} = 5.474(1)$  Å,  $b_{1'LB-a} = 15.684(2)$  Å,  $c_{1'LB-a} = 15.440(2)$  Å,  $\alpha_{1'LB-a} = 90.84(1)^\circ$ ,  $\beta_{1'LB-a} = 107.57(2)^\circ$ ,  $\gamma_{1'LB-a} = 87.54(2)^\circ$ ,  $V_{1'LB-a} = 1262.6(4)$  Å<sup>3</sup> (Figure S9). The cell volume and parameters suggested a relationship to the structure of **1**, but there was insufficient information in the pattern to permit an ab initio structure solution of **1'**.

The clear structural change in going from **1** to **1'** upon desolvation was further explored using  $^{13}C$  CP MAS NMR spectroscopy, which is a powerful probe for determining local structural changes in diamagnetic framework materials exhibiting significant structural disorder.<sup>26,36,47</sup> The resonances in the range 125.7–174.6 ppm in the  $^{13}C$  CP MAS NMR spectrum of **1** (Figure 2) can be assigned to the coordinated TBAPy and to the encapsulated guest dioxane (65.5 ppm) and DMF (167.4 ppm) molecules. In **1** there is a single carbonyl carbon resonance at 174.6 ppm, consistent with the observation of only one crystallographically distinct carboxylate in the

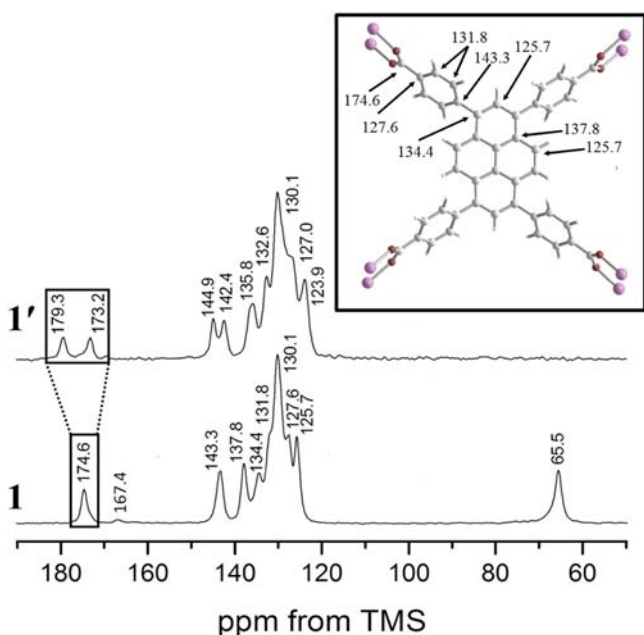


**Figure 2.** Solid-state  $^{13}\text{C}$  CP MAS NMR spectra of (bottom) **1** and (top) **1'** measured at room temperature. The assignment of the resonances in **1** is consistent with the expected resonances corresponding to the TBAPy ligand (inset; numbers given are  $^{13}\text{C}$  resonances in ppm for various carbons). The resonances at 65.5 and 167.4 ppm in **1** correspond to the encapsulated dioxane and DMF molecules, respectively. The resonance at 174.6 ppm (enclosed in a black box) corresponds to the carbonyl carbons of the equivalent carboxylate groups of the TBAPy ligand. Upon desolvation, the resonances corresponding to the encapsulated guest molecules disappear. The observed splitting of the carboxylate resonance in **1** into two peaks in **1'** (enclosed in a black box) shows that two different chemical environments for the  $-\text{COO}$  groups of TBAPy are present, consistent with the simulated and refined crystal structure. Atom colors: pink, Zn; gray, C; red, O; white, H.

structure and comparable to the  $\text{C}_{\text{carbonyl}}$  resonances of other carboxylate-based MOFs.<sup>26,47</sup> The resonance at 143.3 ppm corresponds to the single quaternary carbon attached to the pyrene core (Figure 2). Upon desolvation to afford **1'**, the resonances corresponding to guest molecules are absent, confirming their complete removal. As can be seen from the spectrum of **1'**, there are two resonances at 173.2 and 179.3 ppm corresponding to two nonequivalent  $-\text{COO}$  moieties. The quaternary carbon resonance at 143.3 ppm is also split, leading to additional features at 142.4 and 144.9 ppm, potentially indicating structural nonequivalence of the benzoate groups in the desolvated structure. This observed splitting of the carboxylate and quaternary carbon peaks attached to the pyrene core in the  $^{13}\text{C}$  CP MAS NMR spectrum of **1'** suggests that there are two different chemical environments for the pyrene ligand.

It is noted that framework **1** was stable after standing in air for a month (Figure S11) and could be recovered by exposing **1'** to air and dioxane vapor or immersing it in liquid dioxane overnight, as confirmed by PXRD (Figure S12), TGA (Figure S13), and elemental analysis (section 5 in the SI).

**Simulations and Rietveld Refinement of 1'.** The clear loss of long-range order and structural equivalence of the metal-coordinating benzoate groups that occurs upon desolvation of **1** made determination of the structure of the desolvated phase **1'** extremely difficult. We thus employed MD simulations to

reveal the nature of this structural transformation. Figure 3 shows the structures obtained for the four most important stages among the seven stages described in section 11 in the SI. The GAFF force field<sup>48</sup> was applied to the TBAPy ligand, and the Zn–O force-field terms were validated by reproducing several Zn carboxylate frameworks in addition to **1** (full details of the force field can be found in section 11 in the SI). The Velocity Verlet integration scheme with a time step of 1 fs was used for the MD simulations. The temperature set in the simulations was 298 K, and 10 ps of dynamics with prior equilibration for another 10 ps in each simulation was adequate for structural comparisons. Simulated removal of the coordinated water from the structure of **1** induced significant changes in coordination around the Zn ions (e.g., Figure 3a), but the calculated powder patterns did not resemble the experimental results (e.g., Figure 3b). The force-field terms responsible for retaining the square-pyramidal Zn coordination and paddlewheel structure are much weaker than the Coulombic interactions between the Zn ions and the O atoms of nearby carboxylate groups. When the water ligands are removed, the dominant interactions between the Zn ions and O atoms possess spherical symmetry and thus favor the formation of Platonic coordination polyhedra (tetrahedra, octahedra, cubes); in combination with the constraints imposed by the ligand, this produces several Zn coordination environments. A series of simulations starting from such a disordered structure were carried out wherein the simulation cell parameters were fixed to those obtained from the Le Bail fit of **1'** (i.e., **1'LB-a**) and the following general conditions were applied: (1) the square-pyramidal force-field terms were removed (Figure 3c); (2) the tetrahedral force-field terms were included where compatible with the Zn coordination, and the simulation cell parameters were allowed to change (Figure 3d); (3) a new simulation cell was defined from a part of the structure with tetrahedral Zn coordination obtained in (2) (green box in Figure 3d), and a final simulation was run to relax this new cell to obtain the structure of **1'** (Figure 3e). This structure gave a calculated PXRD pattern remarkably similar to the experimental one (Figure 3f).

In the tetrahedral Zn ions formed following the loss of the water molecules from the axial positions of the paddlewheels (Figure 4a,b), the Zn coordination is completed by coordination from carboxylate groups originally forming paddlewheels in the adjacent layers of **1**. Two of the four carboxylate groups in each paddlewheel shift to bridging positions, coordinatively cross-linking opposite layers, while the remaining two carboxylate groups continue to bridge the original Zn–Zn paddlewheel (Figure 4c; see section 11 in the SI for structural transformation details). The final cell obtained from the simulations contains two  $\text{Zn}_2(\text{TBAPy})$  formula units (consistent with bulk analysis), is monoclinic [ $P2_1/m$ ,  $a_{1i} = 14.654(6)$  Å,  $b_{1i} = 33.045(4)$  Å,  $c_{1i} = 4.798(2)$  Å,  $\beta_{1i} = 87.32(4)^\circ$ ,  $V_{1i} = 2321.0(8)$  Å<sup>3</sup>], and is related to the cell of as-made **1** [ $a_{1i} \approx 2a_1$ ,  $b_{1i} \approx 2b_1$ , and  $c_{1i} \approx c_1/2$  with  $V_{1i} \approx 2V_1$  (Table S2)]. The cell parameters obtained from the Le Bail fit provided a sufficient constraint to prevent loss of order in the MD calculations as the Zn coordination was changed, demonstrating the power of combining calculation and diffraction methods. A detailed comparison of the simulated PXRD pattern with the experimental pattern reveals an increased number of sharper Bragg peaks (Figure 3f and Figure S14), indicating a greater degree of order in the simulated structure compared to experiment; thus, the

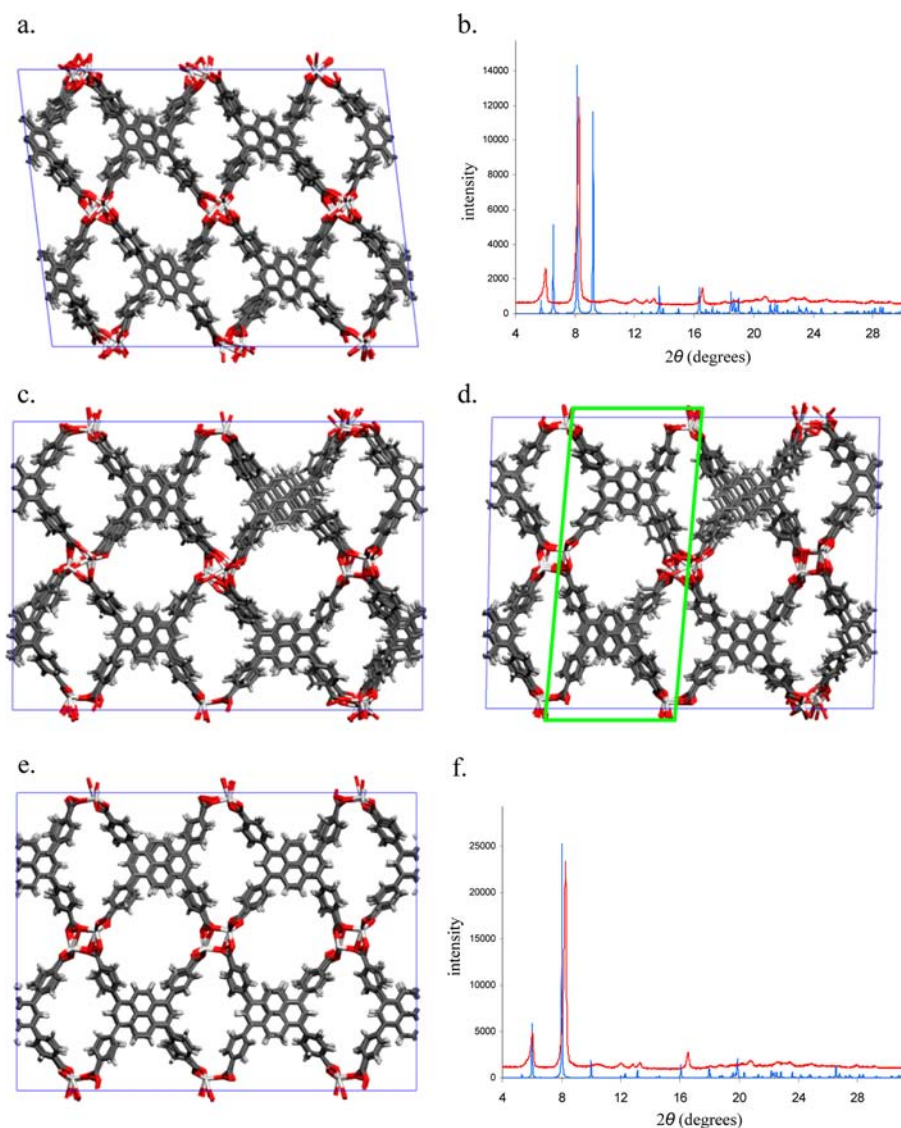


**Figure 3.** Essential stages in the series of simulations that gave rise to the idealized structure of  $1'$ . (a) Removal of the solvent and coordinated water results in disordered Zn coordinations. (b) Comparison of the simulated PXRD pattern for the structure from (a) (blue) and the experimental pattern (red), demonstrating the significant difference of this structure with experimental one. (c) Structure obtained after simulations in which the cell parameters were fixed to values obtained from experiment but changes in Zn coordination were allowed without destroying the overall structure. (d) Structure obtained after simulations in which tetrahedral Zn coordination was applied where structurally compatible and the cell parameters were allowed to relax. (e) Idealized structure of  $1'$  obtained by simulations of a new cell constructed from the highlighted area in (d) in which the cell shape was allowed to change. (f) Comparison showing the much improved correspondence of the simulated PXRD pattern of the structure from (e) (blue) with the experimental pattern (red). Atom colors: gray, C; red, O; white, H.

simulation yielded an idealized structure for  $1'$ , hereafter called  $1'_i$ .

The energies obtained from MD simulations using different force fields for the Zn coordination are not easily comparable because the use of different force-field terms gives rise to geometry- and parameter-dependent differences in the absolute energies. Hence, the change in metal coordination geometry upon ligand removal was quantitatively validated by density functional theory (DFT) calculations. Energies were calculated using DFT as implemented in the CP2K/Quickstep<sup>49</sup> program with the BLYP functional, TZVP-MOLOPT basis sets,<sup>50</sup> and the Grimme-D3 dispersion correction (DFT-D3).<sup>51</sup> The fully optimized DFT structure of  $1'_i$  (Figure 3e) was found to be lower in energy by 3.1 eV per unit cell relative to the DFT-optimized structure of  $1$  with the solvent removed, in which square-planar coordination geometry was retained during

optimization. This is consistent with the known coordination preferences of Zn(II).

The idealized cell of  $1'_i$  that emerged from the MD calculations was used to obtain an improved Le Bail fit (denoted  $1'_{LB-b}$ ; see Figure S9) of the experimental PXRD pattern, resulting in a closely related triclinic  $P1$  threefold supercell [ $a_{1'_{LB-b}} = 14.807(1) \text{ \AA}$ ,  $b_{1'_{LB-b}} = 31.484(2) \text{ \AA}$ ,  $c_{1'_{LB-b}} = 12.644(1) \text{ \AA}$ ,  $\alpha_{1'_{LB-b}} = 94.354(9)^\circ$ ,  $\beta_{1'_{LB-b}} = 95.83(1)^\circ$ ,  $\gamma_{1'_{LB-b}} = 89.582(5)^\circ$ ,  $V_{1'_{LB-b}} = 5846.8(9) \text{ \AA}^3$ ;  $P1$ :  $a_{1'_{LB-b}} \approx c_{1'}$ ,  $b_{1'_{LB-b}} \approx 2b_{1'}$ ,  $c_{1'_{LB-b}} \approx 4a_{1'}/3$ ]. This is the smallest supercell that gives the most realistic approximation of the increased extent of disorder in the experimentally observed PXRD pattern of  $1'$  over the idealized simulated unit cell, and it enabled improved fitting of the broader features, particularly centered at  $d \approx 8.4 \text{ \AA}$ . A rigid-body structural refinement ( $1'_{RV}$ ) starting from this supercell and treating the 12 Zn centers and six TBAPy ligands

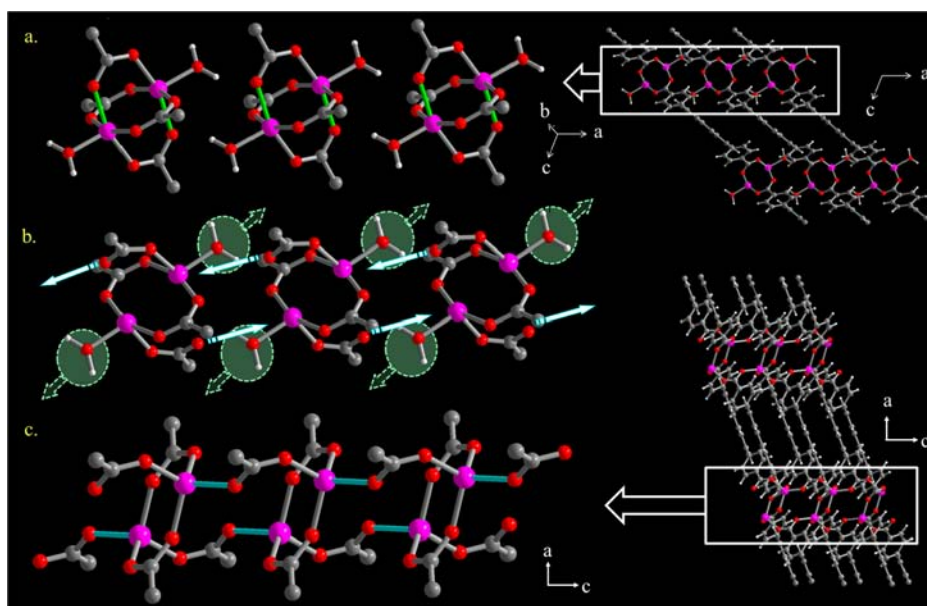


**Figure 4.** Connectivity changes associated with desolvation of **1** to give **1'**. (a) Paddlewheel  $Zn_2$  units in **1**. Each Zn ion has a square-pyramidal geometry in which the equatorial plane is completed by four carboxylate O atoms of TBAPy ligands and the axial position is occupied by a  $H_2O$  molecule. The Zn–O bonds colored in green are the ones that break in step 1, allowing rotation of the carboxylates around their C–O bonds. (b) Step 1: removal of the coordinated  $H_2O$  molecules from the axial positions of the Zn ions in **1** leads to a reorganization of the coordination environment of each  $Zn_2$  unit. Two of the four carboxylate groups in each  $Zn_2$  motif remain bridging within that  $Zn_2$  unit, while the other two shift to bridging positions between one Zn ion in that unit and another Zn ion in a different  $Zn_2$  unit located in an adjacent layer. (c) Step 2: the formation of Zn–O bonds (colored in sky blue) leads to the connection of neighboring  $Zn_2$  units, thus forming 1D Zn–O chains. The Zn ions in **1'** have tetrahedral geometry. Atom colors: pink, Zn; gray, C; red, O; white, H.

independently further demonstrated that this model can properly account for the most intense peaks (Figure 5). It was possible to refine the positions of the Zn ions and TBAPy ligands as well as the ligand orientation, including the dihedral angles describing the benzoate pendant groups. The refined structure  $1'_{Rv}$  (Figure 5b,c) indicates that the relative orientations of the phenyl groups contribute most to the observed disorder in **1'**: while the spacing of the pyrene cores remains  $\sim 4.1$  Å, the dihedral angles of the phenyl rings relative to the pyrene core vary between 4 and  $62^\circ$ , compared with the  $60^\circ$  angles in  $1'_i$ ; also, the carboxylate groups are rotated  $\pm 47^\circ$  out of the plane of the phenyl rings, while in  $1'_i$  they are nearly coplanar (Figure 5b,c). The rotation of the carboxylate groups in  $1'_{Rv}$  maintains the tetrahedral Zn coordination of  $1'_i$  (Figure 5c), although the rotation of the phenyl rings gives rise to unrealistically short H...H contacts between phenyl hydrogens of the stacked TBAPy ligands. This suggests that a different and possibly larger supercell or fractional occupations would be needed to properly describe the disorder fully on the basis of this structural motif. However, it is doubtful that the PXRD data provide enough information to refine such a large and unconstrained model, as refinement against the experimental PXRD pattern shows little discrimination in the agreement factors for different phenyl conformations.

The structure of  $1'_i$  and the behavior of the MD simulations of desolvation thus offer an explanation for the disorder observed in **1'**. The change from a pair of square-planar Zn paddlewheels in **1** after water removal, which are identical under translation (Figure 4a), to the pair of translationally nonequivalent tetrahedral Zn coordinations in  $1'_i$  (Figure 4c) can occur in two ways (Figure S15). These two outcomes are trivially identical, being related through translation by half a cell; however, if during the transformation from **1** to **1'**

different areas of the same crystallite were to start forming the tetrahedrally coordinated Zn centers independently, there would be a 50% probability of forming the structure “in phase” with adjacent areas. MD simulations of structures based on  $1'_i$  confirmed that the flexibility of the structure is such that these out-of-phase regions can coexist at short separations and with only small energy penalties (section 11 in the SI).

**Transformation from **1** to **1'**.** Here we refer to the transformation from **1** to **1'** (rather than to  $1'_i$  or  $1'_{Rv}$ ), as most of the points are common to both the simulated and refined structures. The comparison described below was performed using the  $1'_i$  structure.

The simulations indicated that removal of the coordinated  $H_2O$  molecules from the paddlewheel units of **1** induces breakup of the paddlewheels and subsequent cross-linking of adjacent layers through dimers of tetrahedrally coordinated Zn (Figure 6a–d). The arrangement of the 2D layers in **1** is such that the Zn ions and carboxylate groups in different layers can bond with each other if the layers rotate (Figure 6e–h). The pyrene cores in **1'** are rotated relative to those in **1** in such a way that one end of each ligand remains near the original Zn ions while the other end rotates closer to an adjacent Zn–Zn pair and binds to them rather than the original cations (see videos S1 and S2 in the SI and Figure 6e–h). In **1'**, the ligands all rotate the same way, but the doubling of the unit cell is caused by half of the ligands remaining anchored at one end while the other half remain anchored at the other end (Figure 6e–h and Figure S16). The formation of tetrahedral coordination around the Zn ions and the formation of Zn–O bonds between the layers (Figure 6e–h) increases the dimensionality of the structure from 2D to 3D upon desolvation (Figure 7a–d and Figures S17 and S19). The transformation from **1** to **1'** is enabled by a number of specific

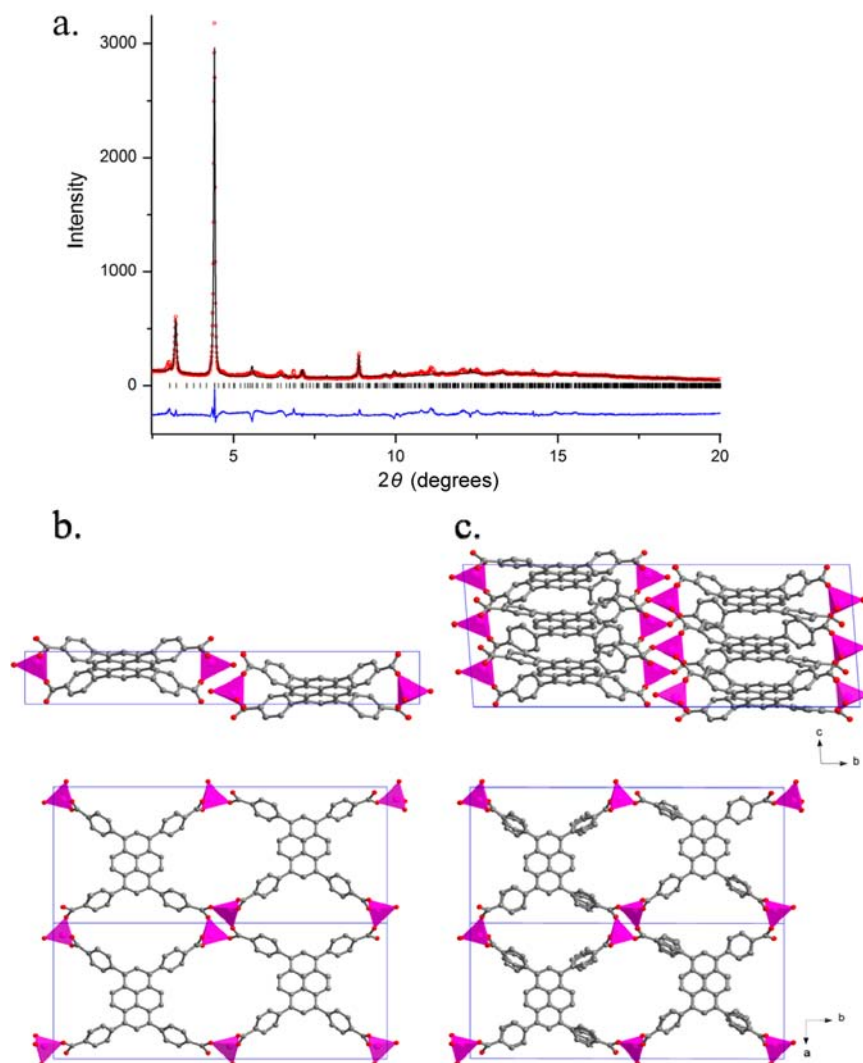


**Figure 5.** (a) Final fit (Rietveld refinement) for a rigid-body structural refinement of the PXRD pattern of **1'** with agreement factors  $R_{wp} = 10.8\%$ ,  $R_p = 8.18\%$ , and  $\chi^2 = 6.28$  and cell parameters  $a_{1'_{Rv}} = 14.81(1)$  Å,  $b_{1'_{Rv}} = 31.47(1)$  Å,  $c_{1'_{Rv}} = 12.67(4)$  Å,  $\alpha_{1'_{Rv}} = 94.1(3)^\circ$ ,  $\beta_{1'_{Rv}} = 95.9(3)^\circ$ ,  $\gamma_{1'_{Rv}} = 89.5(1)^\circ$ , and  $V_{1'_{Rv}} = 5860(21)$  Å<sup>3</sup> (triclinic,  $P1$ ): final observed (red  $\circ$ ), calculated (solid black lines), and difference (solid blue line). (b, c) Structures of (b) **1'**<sub>i</sub> obtained by MD simulation of the desolvation of **1** and (c) **1'**<sub>Rv</sub> obtained from rigid-body structural refinement of the experimental PXRD data of **1'**: (top) views parallel to  $[100]$  showing the tripled unit cell length along  $c$  in **1'**<sub>Rv</sub>, allowing more disorder to be incorporated into the model; (bottom) views along  $[001]$  showing the tetrahedral Zn coordination in both structures and the broader range of phenyl ring orientations in **1'**<sub>Rv</sub>. Atom colors: pink, Zn; gray, C; red, O.

structural changes arising from the coordination lability of Zn and the flexibility of the benzoate groups bound to the pyrene core, which are discussed in detail below.

**a. Change in Metal Coordination Geometry.** In both **1** and **1'**, each TBAPy ligand is bonded to eight Zn ions and each Zn ion is bound to four TBAPy ligands (Figure 7a–d). In the paddlewheel units in **1**, all of the TBAPy ligands necessarily coordinate in a *syn,syn* fashion (Figure 7a,b). In contrast, pairs of Zn centers in **1'** show *syn,anti* coordination to six TBAPy ligands, each of which is bound to six different Zn<sub>2</sub> units (Figure 7c,d and Figure S18). The formation of the Zn–O bonds between the layers of **1** shortens the closest Zn–O distance between neighboring Zn<sub>2</sub> units from 4.301(4) to 2.006(7) Å in **1'** (Figures S20 and S21). The Zn–Zn distance of 6.813(3) Å between two discrete Zn<sub>2</sub> units in **1** is reduced to 4.798(2) Å in **1'**, while the Zn–Zn separation within a given Zn<sub>2</sub> unit increases from 2.936(2) Å in **1** to 3.703(1) Å in **1'** (Figures S20 and S21).

**b. Distortions of the TBAPy Ligand.** As illustrated in Figure S22, the separations between the benzoate centroids at positions 1 and 3 and at positions 6 and 8 of one single TBAPy ligand in **1** are both 7.288(1) Å. In **1'**, the benzoate groups at positions 1 and 3 link the two metal centers of a former paddlewheel of **1** (colored in green in Figure S22) with a distance of 7.550(7) Å between centroids, while the benzoate groups at positions 6 and 8 form bonds between Zn ions from two previously discrete Zn<sub>2</sub> paddlewheels (colored in orange in Figure S22) with a distance of 7.230(7) Å between centroids. The asymmetry of the binding modes induces asymmetric distortions of the TBAPy ligand: the angles formed by the pyrene carbon, phenyl centroid, and carboxylate carbon of each pendant benzoate group are 178.22(0)<sup>o</sup> in **1** and 172.71(4)/177.85(2)<sup>o</sup> in **1'** (Figure S22), while the dihedral angles formed by the pyrene core and the pendant benzoate groups (aromatic C<sub>6</sub>H<sub>4</sub> planes) are 120.29(7)<sup>o</sup> in **1** and 110.07(3)/116.61(1)<sup>o</sup> in **1'** (Figure S23). The rotation of the pyrene cores and the

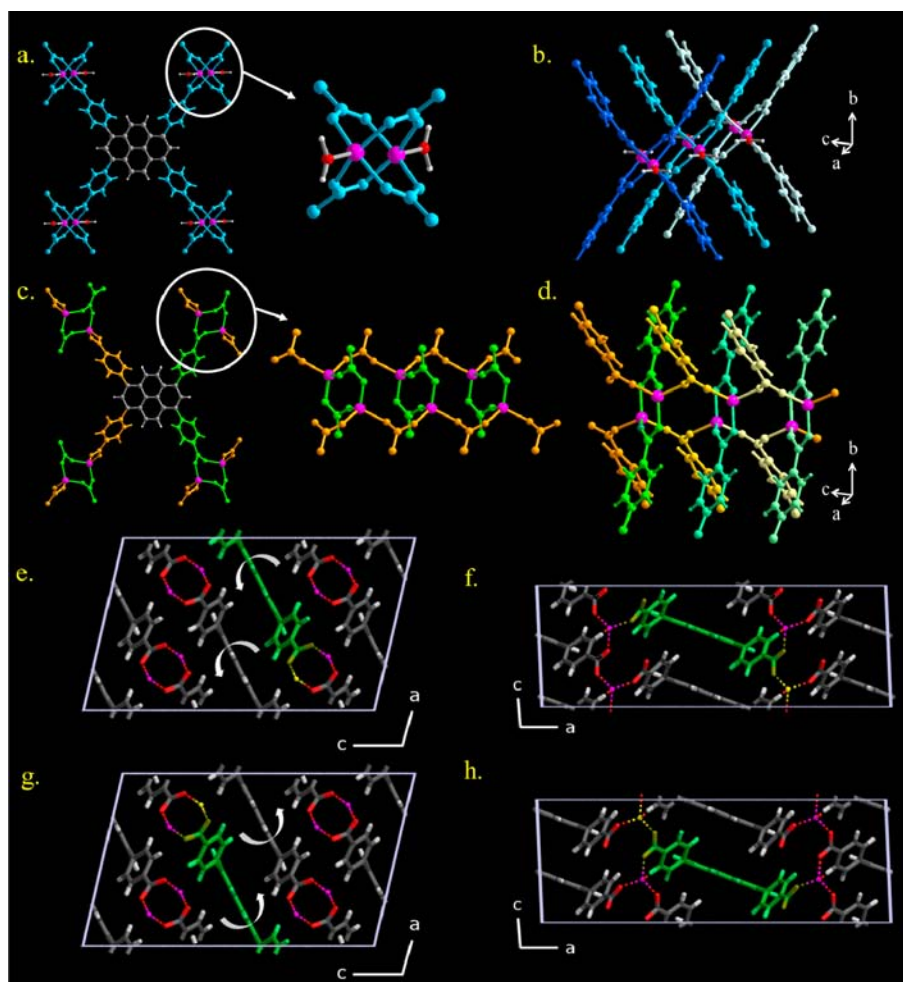


**Figure 6.** (a) Binding mode of the TBAPy ligands in **1**. Each ligand is coordinated to eight independent Zn atoms in syn,syn mode, and all of the benzoate fragments (colored in sky blue) are equivalent. (b) Three unconnected adjacent paddlewheel units in neighboring layers in **1** (the different shades of blue distinguish the three different layers). (c) Illustration of the TBAPy ligand within **1'**. Each ligand is coordinated to eight Zn ions, as in **1**. However, two of the carboxylates of the TBAPy ligand (colored in green) bind to two Zn ions within the same  $Zn_2$  unit (originating from paddlewheel units in **1**), while the other two (colored in orange) link two Zn ions from neighboring  $Zn_2$  units in neighboring layers, giving rise to 1D Zn–O chains. (d) Local environment of the Zn ions in **1'**. The two specific carboxylate modes are colored in green/pale green and orange/pale yellow. The orientation of the TBAPy ligands around the Zn ions gives rise to a 3D network with 1D Zn–O chains connecting the 2D layers in **1**. (e–h) Rotation of the pyrene cores about axes perpendicular to the plane of the page in **1** (e, g) to afford the structure of **1'** (f, h), in which the rotation causes doubling of the *b* axis. In (e) and (g), the view is of two successive unit cells along the positive *b* axis of **1**, while for clarity, (f) and (h) show the top and bottom halves viewed along the negative *b* axis of the unit cell of **1'** respectively. The benzoates at one end of each ligand remain anchored to the coordinated zinc ions shown in yellow (in this view, only one of two benzoates at the anchored end of the ligand is visible, as they are superimposed on each other) while the plane of the pyrene rotates (counterclockwise in these views); in the top half of the cell (e), the ligands are anchored to the Zn ions on the right of the unit cell, while for the bottom half of the cell (g), they are anchored on the left of the unit cell. An example of a rotating ligand is shaded green in each case, with the anchoring Zn ions shown in yellow. This Zn cation remains coordinated to the carboxylate, which upon rotation bridges to the purple Zn cation from the layer below. The nonanchored end of the ligand does not remain bound to any of the cations to which it is bound in **1**. Instead, it coordinates to a Zn ion in the Zn pair from an adjacent layer. The loss of translational symmetry caused by the two sets of rotating ligands results in the doubling of the unit cell perpendicular to the page. The angle between the pyrene plane and the horizontal translation vector between the Zn–Zn centroids in these views is reduced from  $63.45^\circ$  in **1** to  $19.14^\circ$  in **1'**. The angle between the pyrene planes and the translation vector along the pores (parallel to the near-vertical cell vectors in these views) increases from  $39.60^\circ$  in **1** to  $68.18^\circ$  in **1'**.

formation of the 1D Zn–O chains in **1'** brings the benzoate fragments of two neighboring TBAPy ligands closer together than they are in **1** [4.798(1) vs 6.813(1) Å] (Figure S24 and Figure 8 right).

The observed changes in coordination geometry indicate that the reversible transformations between **1** and **1'** upon removal and addition of  $H_2O$  are facilitated by the flexible coordination mode of the carboxylate groups and the flexibility of the TBAPy ligand, which enable the pyrene core to rotate and change the

dihedral angles between the pyrene core and pendant benzoate groups (see videos S1 and S2 in the SI). This is further supported by the  $^{13}C$  CP MAS NMR spectra of **1'**, in which two benzoate coordination modes are clearly observed. This is entirely consistent with the simulated structure wherein one carboxylate bridges the same  $Zn_2$  unit forming a paddlewheel in **1** while the second links two adjacent  $Zn_2$  units originally in different layers to form the 1D chains, extending the structure in three dimensions.

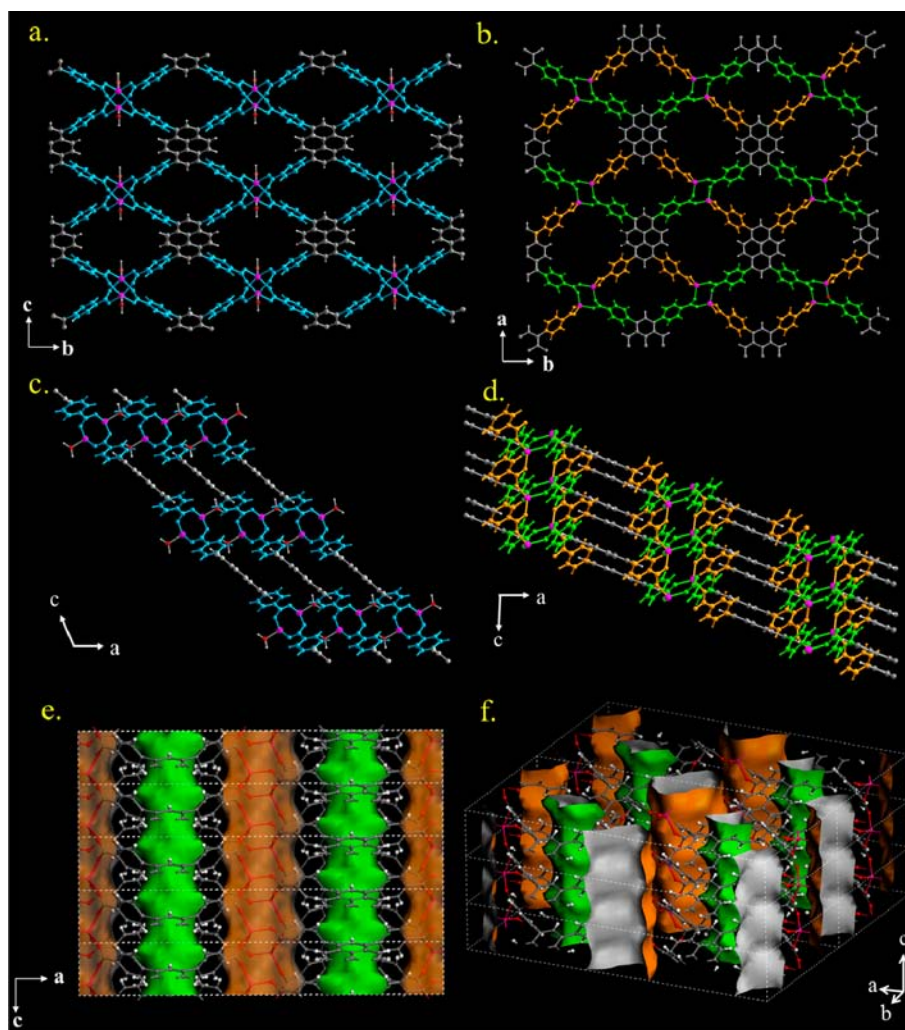


**Figure 7.** (a) Ball-and-stick representation of **1** along the *a* axis, showing that the orientation of the TBAPy ligands around the Zn paddlewheels produces two distinct channels with comparable dimensions. (b) Ball-and-stick illustration of **1'** along the *c* axis, showing that upon desolvation the benzoate fragments in **1** [colored blue in (a)] no longer bind to Zn in an equivalent manner. The green-colored benzoate groups bind to the same  $Zn_2$  units as in **1**, while the orange-colored benzoates link two neighboring  $Zn_2$  units to form 1D Zn–O chains running along the *c* axis. The orientation of the TBAPy ligands around the tetrahedrally coordinated Zn ions results in the formation of two distinct channels with different sizes. (c) Ball-and-stick representation of **1** along the *b* axis, showing three distinct layers that are stacked via  $\pi$ – $\pi$  stacking interactions between the pyrene cores. (d) View of **1'** along the *b* axis, showing the formation of the 1D Zn–O chains running along the *c* axis to link the layers and the orientation of the TBAPy ligands around the 1D chains. The numbers of  $Zn_2$  units and TBAPy ligands presented in (d) are equal to those presented for **1** in (c); the appearance of the extra ligand is due to the corrugation of the layers. (e) Connolly surface representation of **1'** viewed along the *b* axis, showing the different sizes of the pores (smaller pores in green and larger pores in orange). (f) Connolly surface representation of **1'** in a 3D view. Atom colors: pink, Zn; gray, C; red, O; white, H.

The changes in bonding between the different pairs of Zn ions in **1'** generate 1D Zn–O chains running parallel to the crystallographic *c* axis that are cross-linked by the TBAPy ligands (Figures 6c,d and 7b,d,e). The rotation of the pyrene cores in **1'** changes the cross-sectional areas of the pores with respect to **1** (Figure 7e,f and Figure S25). In contrast to **1**, there are two types of pores with differing shapes in **1'**: larger circular pores having a cross section of  $9.0 \text{ \AA} \times 8.0 \text{ \AA}$  and smaller elliptical pores with dimensions of  $5.8 \text{ \AA} \times 5.3 \text{ \AA}$  (calculated with HOLE; Figure 7e,f). The total accessible volume of **1'** calculated from the Connolly surface using the Materials Studio 5.0 modeling package with a probe radius of  $1.0 \text{ \AA}$  was found to be 39.0%. The rotation of the pyrene cores is accompanied by an increase in their mutual overlap, and although their interplane spacing increases from  $4.533(9) \text{ \AA}$  in **1** to

$4.798(2) \text{ \AA}$  in **1'**, it is still within the range of spacings for  $\pi$ – $\pi$  stacking interactions (Figures S24 and S25b).<sup>52,53</sup>

**Optical Properties of **1** and **1'**.** The polyaromatic and highly fluorescent pyrene core of the TBAPy ligand gives emissive properties that change under the structural transformation from **1** to **1'**.<sup>16,17,54</sup> Upon desolvation (Figure S26), the color of **1'** becomes darker yellow. Both frameworks display strong absorption bands from 200 to 500 nm arising from the  $\pi$ – $\pi^*$  transition of the aromatic rings (Figure S27).<sup>55</sup> The absorbance maxima of desolvated **1'** are slightly red-shifted (30 nm) from those of **1**. The fluorescence properties of **1** and **1'** at an excitation wavelength of 417 nm are compared with the emission profile of  $H_4TBAPy$  in Figure 8. **1** displays an emission band at 478 nm, which is blue-shifted relative to the 529 nm band of  $H_4TBAPy$ . The emission intensity of **1** is quenched ( $I = 0.65$ ) compared with that of free  $H_4TBAPy$  ( $I =$

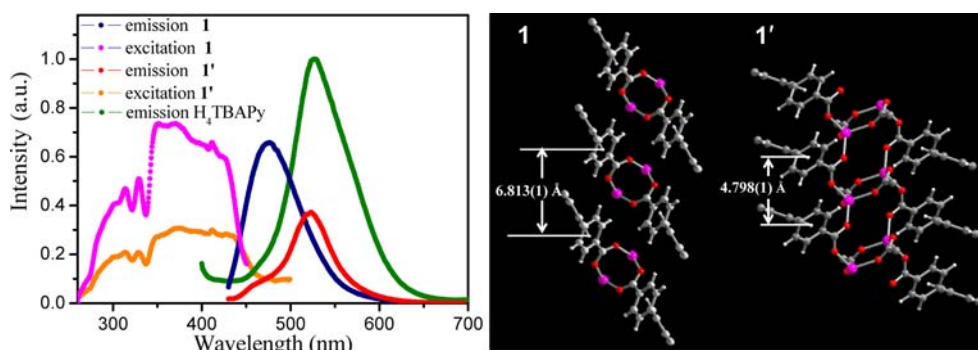


**Figure 8.** (left) Fluorescence emission and excitation spectra of **1**, **1'**, and free  $H_4TBAPy$  collected in the solid state at room temperature in sealed quartz capillaries with a diameter of 0.7 mm. The emission intensities of **1**, **1'**, and  $H_4TBAPy$  have been normalized to the maximum emission band of  $H_4TBAPy$  for ease of comparison. (right) Distances between the benzoate phenyl groups in **1** and **1'**. The quenching and red shift observed upon desolvation are attributed to the more pronounced face-to-face interactions between the phenyl groups of the TBAPy ligands in **1'**, as the distance between them is 4.798(1) Å vs 6.813(1) Å in **1**. The pyrene–pyrene distance in **1'** [4.798(2) Å] is slightly larger than that in **1** [4.533(9) Å]. Atom colors: pink, Zn; gray, C; red, O; white, H.

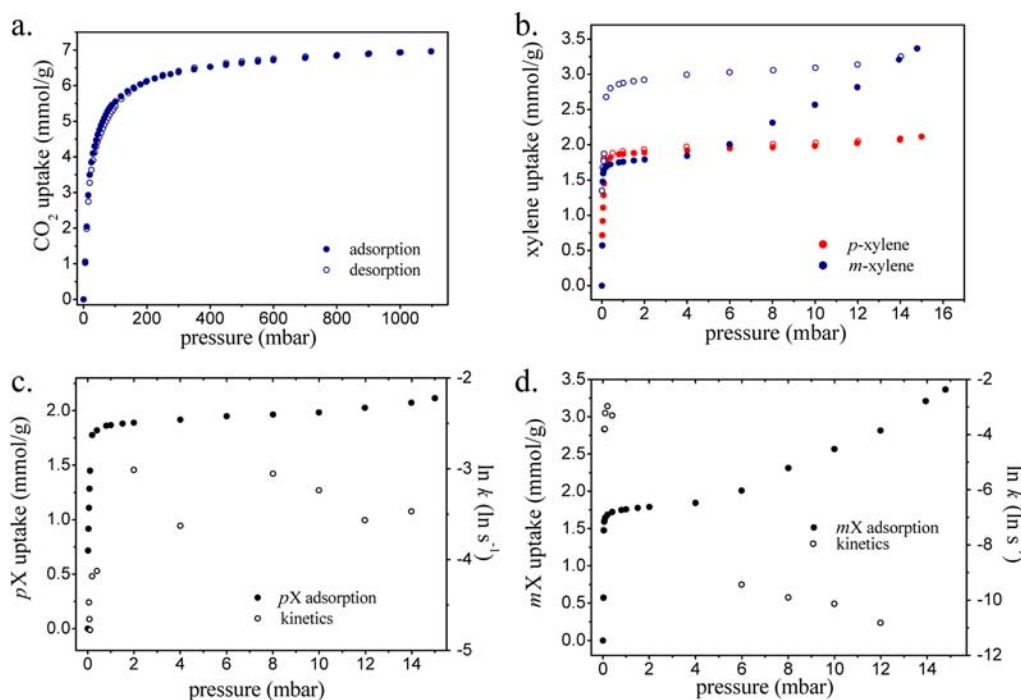


**Figure 9.** (a) Type-I  $CO_2$  isotherm measured on **1'** at 195 K and 1 bar. (b) *m*-Xylene (*mX*) and *p*-xylene (*pX*) isotherms for **1'** collected at 303 K (●, adsorption; ○, desorption; red, *pX*; blue, *mX*). (c, d) Variation of sorption kinetics ( $\ln k$ ; right-hand axis, ○) and uptake (left-hand axis, ●) with pressure for (c) *pX* and (d) *mX*.

**1**). The absence of a ligand-to-metal charge transfer (LMCT) band indicates that the observed emission of **1** is generated solely by the ligand.<sup>56,57</sup> Upon desolvation, the emission profile of **1'** is red-shifted by 47 nm compared with **1**. The red shift and quenching ( $I = 0.38$ ) of the fluorescence emission of **1'** are attributed to the structural changes that occur upon removal of the guest molecules from the cavities and the coordinated  $H_2O$  molecule from each Zn center. The quenching of the emission profile is attributed to the large change in the face-to-face interactions of the benzoate groups (Figure 8), which are closer in **1'** than in **1** [4.798(1) Å in **1'** vs 6.813(1) Å in **1**], rather than the less affected pyrene–pyrene interactions [4.798(2) Å in **1'** vs 4.533(9) Å in **1**] (Figure S24).

**Porosity and Guest Response.** The permanent microporosity of **1'** was demonstrated by a type-I  $CO_2$  sorption isotherm at 195 K following activation at 110 °C under

dynamic vacuum ( $10^{-6}$  mbar overnight) (Figure 9a). The Brunauer–Emmett–Teller (BET) surface area over the relative pressure range  $p/p^\circ = 0.02–0.22$  was found to be 523(8)  $m^2/g$  (Figure S28), and Dubinin–Radushkevich (DR) analysis<sup>58</sup> gave a pore volume of 0.314  $cm^3/g$  (Table S3 and Figure S29), which is in excellent agreement with the value of 0.329  $cm^3/g$  calculated from the simulated structure of **1'**. This is significantly larger than the pore volume derived from the static structure of **1** after removal of the coordinated  $H_2O$  molecules (0.274  $cm^3/g$ ), further supporting the tetrahedrally coordinated Zn-based structure of **1'** derived from the experimental/modeling approach outlined above. Framework **1'** was also found to be porous to  $CO_2$  and  $CH_4$  at 273 and 298 K at 5 bar (Figure S30b). The isosteric heat of adsorption ( $Q_{st}$ ) of **1'** for  $CO_2$  was found to be 21.0 kJ/mol at zero coverage, with an increase to 24.8 kJ/mol at high  $CO_2$  loading (Figure

S30c). The slight increase in the strength of the interactions between **1'** and CO<sub>2</sub> may occur because the specific pore size of the framework results in interactions with the tetrahedrally coordinated Zn atoms.<sup>59</sup> The  $Q_{st}$  of **1'** for CH<sub>4</sub> was found to be 20.3 kJ/mol at zero coverage, with a slight decrease to 18.4 kJ/mol at high loadings (Figure S30c).<sup>60</sup>

The channel dimensions and polyaromatic pores of **1'** suggested measurement of the vapor sorption isotherms of *m*-xylene (*mX*) and *p*-xylene (*pX*). The similar sizes and physicochemical behavior of the two xylene isomers (*pX*, 7.72 Å × 5.11 Å; *mX*, 7.43 Å × 5.67 Å; Figure S31) make separations based on open-framework materials of interest, with some of the best figures of merit reported for MOF-type structures.<sup>61,62</sup> The dynamical nature of the structure of **1'** produced a clear distinction in the vapor sorption responses to the two guest molecules.

The *mX* and *pX* vapor isotherms were measured for **1'** at 303 K and 15 mbar. The *pX* isotherm (Figure 9b) is type I and reversible and saturates above 2 mbar, reaching a limit of 1.70 *pX* molecules per Zn<sub>2</sub>(TBAPy) formula unit (FU) at 15 mbar. This corresponds to 82.8% of the total pore volume; the reduced filling by *pX* in comparison with CO<sub>2</sub> is assigned to the more complex shape and larger volume of *pX*. The *mX* isotherm is completely different from that measured for *pX*. The *mX* isotherm shows hysteretic behavior, with the uptake reaching a first plateau at 2 mbar followed by a step at higher pressure. The loading at 2 mbar is similar for *pX* (1.53 molecules/FU) and *mX* (1.45 molecules/FU). At 15 mbar, **1'** sorbs 2.71 *mX* molecules/FU, corresponding to a pore volume of 0.414 cm<sup>3</sup>/g, which is 131.8% of the original pore volume (Table 1).<sup>35</sup>

**Table 1. Xylene (*pX* and *mX*) Uptake Data for **1'** Derived from the Vapor Isotherms Collected at 303 K at 2 and 15 mbar**

		2 mbar	15 mbar
<i>pX</i>	uptake (mmol/g)	1.89	2.11
	molecules per Zn <sub>2</sub> (TBAPy)	1.53	1.70
	pore volume (cm <sup>3</sup> /g)	0.231	0.260
	filling of pore volume (%)	73.1	82.8
<i>mX</i>	uptake (mmol/g)	1.79	3.36
	molecules per Zn <sub>2</sub> (TBAPy)	1.45	2.71
	pore volume (cm <sup>3</sup> /g)	0.220	0.414
	filling of pore volume (%)	70.1	131.8

The kinetics of each xylene isotherm were fitted using the stretched exponential (SE) model (see sections 18–20 in the SI). The kinetics of the low- and high-pressure steps for the *pX* and *mX* adsorption are shown in Figure 9c,d. The initial uptake sections for both *pX* and *mX* adsorption [up to 0.4 mbar (0–1.81 mmol/g)] showed fast uptake kinetics with rate constants of (2–5) × 10<sup>-2</sup> s<sup>-1</sup> (see sections 19 and 20 in the SI). The rate constant for *pX* adsorption remained at the same order of magnitude across the isotherm plateau region (see the kinetics plots in sections 19 and 20 in the SI), and the material retained the same structure. The kinetics of the *mX* adsorption was significantly slower after the plateau. The rate constant for *mX* decreased to (2–6) × 10<sup>-5</sup> s<sup>-1</sup> (i.e., almost 1000 times lower) at pressures above 4 mbar, which is consistent with the second uptake region (1.90–3.36 mmol/g) of the *mX* adsorption isotherm. In contrast, the *pX* uptake increased only from 1.89 to 2.11 mmol/g over this pressure range. The plots of ln *k*

versus pressure (Figure 9c,d) clearly show this decrease in rate for *mX* adsorption above 4 mbar. It is worth noting that the duration of the *pX* isotherm was ~2 days, while for *mX* the duration was 10 days. The *mX* and *pX* isotherms in a repeat experiment are shown in Figure S32. The slow kinetics affording the enhanced pore volume derivative of **1'** suggests that the *mX* guest drives a structural transformation in **1'** to allow enhanced loading over that possible in the original porous structure. This further supports the dynamical nature of the porosity provided by TBAPy coordination to Zn<sup>2+</sup>.

## CONCLUSIONS

The combination of the rigid pyrene core with the rotatable benzoate units of the TBAPy ligand affords an open-framework structure that is able to respond dynamically to the species coordinating to the Zn centers and the nature of the guests occupying the channel space. The resultant response to removal of the water ligands initially forming the Zn<sub>2</sub> paddlewheels in as-grown **1** is sufficiently flexible to reduce the crystallinity severely, requiring the integrated use of computer modeling, diffraction data, and locally sensitive NMR spectroscopy to identify the structure of the resulting open framework **1'**. The coordination at the Zn centers in **1'** is satisfied by a dimensionality increase resulting from the formation of Zn–O chains linking the original layers in the purely 2D structure of **1**, enabled through the formation of new bridging bonds by the carboxylates from the TBAPy linker. The resulting 3D open framework has a pore volume in close agreement with that measured experimentally, and the emissive properties are significantly altered by changes in nonbonded interactions upon the structural transformation. **1'** responds in a completely distinct manner to *p*- and *m*-xylene vapors: while the response to *p*-xylene is conventional, the amount of *m*-xylene sorbed far exceeds the available pore volume in **1'**. This unusual uptake plus the slower kinetics and the hysteresis observed when the uptake exceeds the maximum value possible for *p*-xylene suggests that the dynamical nature of the framework permits further structural rearrangement in response to the *m*-xylene guest. Understanding such dynamical processes will require the further development of integrated computational, structural, and spectroscopic work.

## ASSOCIATED CONTENT

### Supporting Information

Crystal structure representations, Le Bail fits, SEM images, UV–vis and IR spectra of **1** and **1'**, TGA profile of **1**, description of the steps that led to **1'** using the simulation methods, stability tests of **1** and **1'**, in situ variable-temperature PXRD study, BET and DR plots for **1'**, CO<sub>2</sub> and CH<sub>4</sub>  $Q_{st}$  values, analysis of the kinetics of the vapor isotherms for the xylene isomers, CIF files of **1** and **1'**, and two videos showing the structural transformation from **1** to **1'**. This material is available free of charge via the Internet at <http://pubs.acs.org>. The supplementary crystallographic data for this paper were deposited with the Cambridge Crystallographic Data Centre (CCDC) as entry CCDC 891428. These data can be obtained free of charge from the CCDC via [www.ccdc.cam.ac.uk/data\\_request/cif](http://www.ccdc.cam.ac.uk/data_request/cif).

## AUTHOR INFORMATION

### Corresponding Author

D.Bradshaw@soton.ac.uk; m.j.rosseinsky@liverpool.ac.uk

**Present Address**

<sup>§</sup>School of Chemistry, University of Southampton, Highfield, Southampton SO17 1BJ, U.K.

**Notes**

The authors declare no competing financial interest.

**ACKNOWLEDGMENTS**

The authors thank the EPSRC for funding under EP/H000925 and the EU for funding (SURMOF). We thank the Diamond Light Source for access to beamline I11 that contributed to the results presented here and Prof. Chiu Tang, Dr. Julia Parker, and Dr. Alistair Lennie for their assistance during the experiment.

**REFERENCES**

- (1) Kitagawa, S.; Kitaura, R.; Noro, S. *Angew. Chem., Int. Ed.* **2004**, *43*, 2334.
- (2) Meek, S. T.; Greathouse, J. A.; Allendorf, M. D. *Adv. Mater.* **2011**, *23*, 249.
- (3) Tranchemontagne, D. J.; Mendoza-Cortés, J. L.; O’Keeffe, M.; Yaghi, O. M. *Chem. Soc. Rev.* **2009**, *38*, 1257.
- (4) Murray, L. J.; Dincă, M.; Long, J. R. *Chem. Soc. Rev.* **2009**, *38*, 1294.
- (5) Furukawa, H.; Ko, N.; Go, Y. B.; Aratani, N.; Choi, S. B.; Choi, E.; Yazaydin, A. O.; Snurr, R. Q.; O’Keeffe, M.; Kim, J.; Yaghi, O. M. *Science* **2010**, *329*, 424.
- (6) Yan, Y.; Lin, X.; Yang, S.; Blake, A. J.; Dailly, A.; Champness, N. R.; Hubberstey, P.; Schroder, M. *Chem. Commun.* **2009**, 1025.
- (7) Li, J.-R.; Kuppler, R. J.; Zhou, H.-C. *Chem. Soc. Rev.* **2009**, *38*, 1477.
- (8) Couck, S.; Denayer, J. F. M.; Baron, G. V.; Remy, T.; Gascon, J.; Kapteijn, F. *J. Am. Chem. Soc.* **2009**, *131*, 6326.
- (9) Stylianou, K. C.; Warren, J. E.; Chong, S. Y.; Rabone, J.; Bacsá, J.; Bradshaw, D.; Rosseinsky, M. J. *Chem. Commun.* **2011**, 47, 3389.
- (10) Lee, J.; Farha, O. K.; Roberts, J.; Scheidt, K. A.; Nguyen, S. T.; Hupp, J. T. *Chem. Soc. Rev.* **2009**, *38*, 1450.
- (11) Wu, C. D.; Hu, A.; Zhang, L.; Lin, W. B. *J. Am. Chem. Soc.* **2005**, *127*, 8940.
- (12) Hwang, Y. K.; Hong, D.-Y.; Chang, J.-S.; Jhung, S. H.; Seo, Y.-K.; Kim, J.; Vimont, A.; Daturi, M.; Serre, C.; Férey, G. *Angew. Chem., Int. Ed.* **2008**, *47*, 4144.
- (13) Horcajada, P.; Serre, C.; Maurin, G.; Ramsahye, N. A.; Balas, F.; Vallet-Regí, M.; Sebba, M.; Taulelle, F.; Férey, G. *J. Am. Chem. Soc.* **2008**, *130*, 6774.
- (14) Imaz, I.; Rubio-Martínez, M.; García-Fernández, L.; García, F.; Ruiz-Molina, D.; Hernando, J.; Puentes, V.; MasPOCH, D. *Chem. Commun.* **2010**, 46, 4737.
- (15) Quartapelle Procopio, E.; Rojas, S.; Padial, N. M.; Galli, S.; Masciocchi, N.; Linares, F.; Miguel, D.; Oltra, J. E.; Navarro, J. A. R.; Barea, E. *Chem. Commun.* **2011**, 47, 11751.
- (16) Allendorf, M. D.; Bauer, C. A.; Bhakta, R. K.; Houk, R. J. T. *Chem. Soc. Rev.* **2009**, *38*, 1330.
- (17) Cui, Y.; Yue, Y.; Qian, G.; Chen, B. *Chem. Rev.* **2012**, *112*, 1126.
- (18) Cui, Y.; Xu, H.; Yue, Y.; Guo, Z.; Yu, J.; Chen, Z.; Gao, J.; Yang, Y.; Qian, G.; Chen, B. *J. Am. Chem. Soc.* **2012**, *134*, 3979.
- (19) Horike, S.; Shimomura, S.; Kitagawa, S. *Nat. Chem.* **2009**, *1*, 695.
- (20) Rosseinsky, M. J. *Microporous Mesoporous Mater.* **2004**, *73*, 15.
- (21) Uemura, K.; Yamasaki, Y.; Komagawa, Y.; Tanaka, K.; Kita, H. *Angew. Chem., Int. Ed.* **2007**, *46*, 6662.
- (22) Chun, H.; Dytsev, D. N.; Kim, H.; Kim, K. *Chem.—Eur. J.* **2005**, *11*, 3521.
- (23) Zhu, W. H.; Wang, Z. M.; Gao, S. *Inorg. Chem.* **2007**, *46*, 1337.
- (24) Bourrelly, S.; Llewellyn, P. L.; Serre, C.; Millange, F.; Loiseau, T.; Férey, G. *J. Am. Chem. Soc.* **2005**, *127*, 13519.
- (25) Cussen, E. J.; Claridge, J. B.; Rosseinsky, M. J.; Kepert, C. J. *J. Am. Chem. Soc.* **2002**, *124*, 9574.
- (26) Stylianou, K. C.; Heck, R.; Chong, S. Y.; Bacsá, J.; Jones, J. T. A.; Khimyak, Y. Z.; Bradshaw, D.; Rosseinsky, M. J. *J. Am. Chem. Soc.* **2010**, *132*, 4119.
- (27) Ohba, M.; Yoneda, K.; Agustí, G.; Muñoz, M. C.; Gaspar, A. B.; Real, J. A.; Yamasaki, M.; Ando, H.; Nakao, Y.; Sakaki, S.; Kitagawa, S. *Angew. Chem., Int. Ed.* **2009**, *48*, 4767.
- (28) Gould, S. L.; Tranchemontagne, D.; Yaghi, O. M.; Garcia-Garibay, M. A. *J. Am. Chem. Soc.* **2008**, *130*, 3246.
- (29) Winston, E. B.; Lowell, P. J.; Vacek, J.; Chocholeousova, J.; Michl, J.; Price, J. C. *Phys. Chem. Chem. Phys.* **2008**, *10*, 5188.
- (30) Zhang, J.-P.; Chen, X.-M. *J. Am. Chem. Soc.* **2008**, *130*, 6010.
- (31) Moggach, S. A.; Bennett, T. D.; Cheetham, A. K. *Angew. Chem., Int. Ed.* **2009**, *48*, 7087.
- (32) Horike, S.; Matsuda, R.; Tanaka, D.; Matsubara, S.; Mizuno, M.; Endo, K.; Kitagawa, S. *Angew. Chem., Int. Ed.* **2006**, *45*, 7226.
- (33) Seo, J.; Matsuda, R.; Sakamoto, H.; Bonneau, C.; Kitagawa, S. *J. Am. Chem. Soc.* **2009**, *131*, 12792.
- (34) Seo, J.; Bonneau, C.; Matsuda, R.; Takata, M.; Kitagawa, S. *J. Am. Chem. Soc.* **2011**, *133*, 9005.
- (35) Serre, C.; Mellot-Draznieks, C.; Surlblé, S.; Audebrand, N.; Filinchuk, Y.; Férey, G. *Science* **2007**, *315*, 1828.
- (36) Rabone, J.; Yue, Y. F.; Chong, S. Y.; Stylianou, K. C.; Bacsá, J.; Bradshaw, D.; Darling, G. R.; Berry, N. G.; Khimyak, Y. Z.; Ganin, A. Y.; Wiper, P.; Claridge, J. B.; Rosseinsky, M. J. *Science* **2010**, *329*, 1053.
- (37) Kitaura, R.; Seki, K.; Akiyama, G.; Kitagawa, S. *Angew. Chem., Int. Ed.* **2003**, *42*, 428.
- (38) Chen, B.; Liang, C.; Yang, J.; Contreras, D. S.; Clancy, Y. L.; Lobkovsky, E. B.; Yaghi, O. M.; Dai, S. *Angew. Chem., Int. Ed.* **2006**, *45*, 1390.
- (39) Wang, C.-C.; Yang, C.-C.; Yeh, C.-T.; Cheng, K.-Y.; Chang, P.-C.; Ho, M.-L.; Lee, G.-H.; Shih, W.-J.; Sheu, H.-S. *Inorg. Chem.* **2011**, *50*, 597.
- (40) Kim, M.; Cahill, J. F.; Su, Y.; Prather, K. A.; Cohen, S. M. *Chem. Sci.* **2012**, *3*, 126.
- (41) Walton, R. I.; Millange, F.; Le Bail, A.; Loiseau, T.; Serre, C.; O’Hare, D.; Férey, G. *Chem. Commun.* **2000**, 203.
- (42) Du, M.; Li, C.-P.; Wu, J.-M.; Guo, J.-H.; Wang, G.-C. *Chem. Commun.* **2011**, 47, 8088.
- (43) Ghosh, S. K.; Kaneko, W.; Kiriya, D.; Ohba, M.; Kitagawa, S. *Angew. Chem.* **2008**, *120*, 8975.
- (44) Li, H.; Eddaoudi, M.; Groy, T. L.; Yaghi, O. M. *J. Am. Chem. Soc.* **1998**, *120*, 8571.
- (45) Smart, O. S.; Goodfellow, J. M.; Wallace, B. A. *Biophys. J.* **1993**, *65*, 2455.
- (46) Spek, A. L. *J. Appl. Crystallogr.* **2003**, *36*, 7.
- (47) Lee, E. Y.; Jang, S. Y.; Suh, M. P. *J. Am. Chem. Soc.* **2005**, *127*, 6374.
- (48) Wang, J. M.; Wolf, R. M.; Caldwell, J. W.; Kollman, P. A.; Case, D. A. *J. Comput. Chem.* **2004**, *25*, 1157.
- (49) VandeVondele, J.; Krack, M.; Mohamed, F.; Parrinello, M.; Chassaing, T.; Hutter, J. *Comput. Phys. Commun.* **2005**, *167*, 103.
- (50) VandeVondele, J.; Hutter, J. *J. Chem. Phys.* **2007**, *127*, No. 114105.
- (51) Grimme, S.; Antony, J.; Ehrlich, S.; Krieg, H. *J. Chem. Phys.* **2010**, *132*, No. 154104.
- (52) Cornil, J.; dos Santos, D. A.; Crispin, X.; Silbey, R.; Brédas, J. L. *J. Am. Chem. Soc.* **1998**, *120*, 1289.
- (53) Cornil, J.; Beljonne, D.; Calbert, J. P.; Brédas, J.-L. *Adv. Mater.* **2001**, *13*, 1053.
- (54) Bauer, C. A.; Timofeeva, T. V.; Settersten, T. B.; Patterson, B. D.; Liu, V. H.; Simmons, B. A.; Allendorf, M. D. *J. Am. Chem. Soc.* **2007**, *129*, 7136.
- (55) Zhou, Y. X.; Shen, X. Q.; Du, C. X.; Wu, B. L.; Zhang, H. Y. *Eur. J. Inorg. Chem.* **2008**, 4280.
- (56) Fan, J.; Zhu, H. F.; Okamura, T. A.; Sun, W. Y.; Tang, W. X.; Ueyama, N. *New J. Chem.* **2003**, *27*, 1409.
- (57) Dai, J. C.; Wu, X. T.; Fu, Z. Y.; Cui, C. P.; Hu, S. M.; Du, W. X.; Wu, L. M.; Zhang, H. H.; Sun, R. O. *Inorg. Chem.* **2002**, *41*, 1391.
- (58) Tovbin, Y. K. *Russ. Chem. Bull.* **1998**, *47*, 637.

(59) Vaidhyanathan, R.; Iremonger, S. S.; Shimizu, G. K. H.; Boyd, P. G.; Alavi, S.; Woo, T. K. *Science* **2010**, *330*, 650.

(60) Perkins, C. G.; Warren, J. E.; Fateeva, A.; Stylianou, K. C.; McLennan, A.; Jelfs, K.; Bradshaw, D.; Rosseinsky, M. J. *Microporous Mesoporous Mater.* **2012**, *157*, 24.

(61) Alaerts, L.; Kirschhock, C. E. A.; Maes, M.; van der Veen, M. A.; Finsy, V.; Depla, A.; Martens, J. A.; Baron, G. V.; Jacobs, P. A.; Denayer, J. E. M.; De Vos, D. E. *Angew. Chem., Int. Ed.* **2007**, *46*, 4293.

(62) Vermoortele, F.; Maes, M.; Moghadam, P. Z.; Lennox, M. J.; Ragon, F.; Boulhout, M.; Biswas, S.; Laurier, K. G. M.; Beurroies, I.; Denoyel, R.; Roeffaers, M.; Stock, N.; Düren, T.; Serre, C.; De Vos, D. E. *J. Am. Chem. Soc.* **2011**, *133*, 18526.